



# Effects of Cyclic Heat Treatment on Microstructure and Mechanical Properties of 13%Cr-4%Ni Martensitic Stainless Steel

Jai Singh and S.K. Nath

(Submitted August 6, 2019; in revised form March 14, 2020; published online April 21, 2020)

The present work investigates the effects of thermal cycling heat treatment (TCHT) on microstructure and mechanical properties of 13%Cr-4%Ni martensitic stainless steel (13-4MSS). As-received 13-4 MSS was subjected to three different thermal cycling schedules by using a thermo-mechanical simulator (Gleeble 3800). The evolved microstructures were studied at three cycles for each thermal cycling schedule with the help of optical, scanning electron microscopy, x-ray analysis, and transmission electron microscopy. Hardness and notched tensile tests were conducted to further characterize the as-received and processed specimens. This cyclic treatment raised the hardness to 413 HV (for TCHT at 950 °C) from 274 HV (for as-received). A 42% (for TCHT at 950 °C) and 39% (for TCHT at 1050 °C) hike in ultimate tensile strength (UTS) with a slight decline in ductility was observed as compared to the UTS and ductility of as-received steel. The evolved microstructure, dislocation density, and the refinement of martensitic blocks attributed to the enhanced hardness and UTS. The coarsening of laths (observed at 1050 °C) and bimodal lath structure (observed at 950 °C) were also found to control the mechanical properties of the present steel.

**Keywords** 13%Cr-4%Ni steel, characterization, cycling heat treatment, mechanical properties, microstructure

## 1. Introduction

13%Cr-4%Ni martensitic stainless steel (13-4 MSS) finds wide application in hydropower industries due to its excellent mechanical properties and corrosion resistance (Ref 1). Despite the higher strength and corrosion resistance, modern engineering requires more superior properties. The mechanical properties and the process kinetics of the spheroidization of steels strongly depend on the prior austenitic grain size (Ref 2). The finer grain structure possesses higher strength and the coarser the better ductility (Ref 3). Mostly, thermo-mechanical processing treatments are used for the refinement of grains. These techniques are quite difficult and costly due to the complexity in the experimentation (Ref 4). The thermal cycling heat treatment (TCHT), repeated heating and fast cooling around critical temperature, has evolved a good alternative for better refinement and improvement in mechanical properties, in past decades. Thermal cycling was introduced several decades ago for accelerating the kinetics of spheroidization of steel (Ref 5). Thermal cycling can accelerate the process kinetics, and refine the grains (Ref 6).

In the literature, a large number of studies have applied TCHT on different grades of steel with the goal to refine grains and enhance strength coupled with ductility. The TCHT of

eutectoid steels helps in generating active cementite nuclei through lamellar fragmentation and lamellar thickening, and thereby accelerates the spheroidization kinetics of the pearlite (Ref 7). Atomic diffusion is possible between two adjacent lamellas (due to shorter diffusion distance) and plays an important role in accelerating the kinetics (Ref 7, 8). The spheroidization of the pearlite was done for eutectoid steel while performing the TCHT with different parameters by many researchers (Ref 6-12) and thereby obtaining a better combination of strength and ductility. The TCHT is not only limited to eutectoid steel but other steels were also treated by this treatment. Some studies conducted TCHT on the other plain carbon steels, viz. 0.42 wt.% carbon steel (Ref 13), 0.16 wt.% carbon steel (Ref 14), 1.24 wt.% carbon steel (Ref 15), 0.6 wt.% carbon steel (Ref 16), and 0.4 wt.% carbon steel (Ref 17) to modify the microstructure and mechanical properties. These studies observed a similar spheroidization kinetics (as in eutectoid steel) where the spheroidized fraction was governed by the TCHT parameters used in different studies.

Different micro-alloyed steels were also thermally cycled to hike strength without impairing the ductility. The low-carbon alloy steels (0.12%C-0.5 Mn, and 0.08%C-0.5 Mn) (Ref 18), maraging steels (13Ni-15Co-10Mo, 15Ni-25Co-7Mo, 18-Ni maraging steel) (Ref 1), 50CrV4 steel (Ref 19), and Ti-V micro-alloyed steel (Ref 20) were TCHT processed in order to refine the grains and to obtain the increased strength coupled with ductility. Austenitic stainless steels, being impervious to the heat treatment, were thermally cycled to refine the grains in an effective manner. Thermal cycling led to the formation of ultrafine grains in AISI 340L (0.02 wt.% carbon) (Ref 21) which increased the YS to four- to sixfold as per the Hall-Petch relation. A similar effect was observed in the grain refinement and mechanical property variations (Ref 3, 22). These introduced a bimodal structure in which ultrafine grains were embedded in the original micro-sized grain matrix.

Jai Singh, Centre of Nanotechnology, IIT Roorkee, Roorkee, UK 247667, India; and S.K. Nath, Department of Metallurgical and Materials Engineering, IIT Roorkee, Roorkee, UK 247667, India. Contact e-mails: jsingh@nt.iitr.ac.in and indiafnt@iitr.ac.in.

The work on the TCHT of 13-4 MSS has not been addressed in the available literature. It is an attempt to modify the microstructure and improve the mechanical properties of 13-4 MSS by reducing the amount of undesirable delta-ferrite and refining the martensitic blocks by conducting TCHT. Three schedules of TCHT have been conducted on 13-4 MSS at three temperatures 850, 950, and 1050 °C, respectively. A detailed characterization of the evolved microstructure through TCHT is done by using optical microscopy, scanning electron microscopy, transmission electron microscopy and x-ray analysis. The concerned improvement in mechanical properties is discussed in light of the evolved microstructure and refinement of martensitic blocks.

## 2. Experimental Methods

### 2.1 Material

A grade of martensitic stainless steel, i.e., 13%Cr-4%Ni martensitic stainless steel (13-4 MSS), is selected in this research. The ASTM nomenclature for 13-4 MSS is ASTM

A743 CA-6NM. Bharat Heavy Electricals Limited Haridwar, India, has provided this material in the form of billets for research purpose. The chemical composition of the as-received (13-4 ASR) steel was examined with a Thermo Jarrell Ash Spark Emission Spectroscope. 13-4 ASR composed of 0.07% carbon, 13.51% chromium, 3.35% nickel, 0.64% silicon, 0.62% manganese, 0.01% phosphorous, 0.02% sulfur, 0.06% copper, and 0.32% molybdenum by weight in iron (Fe) matrix.

### 2.2 Thermal Cycling Heat Treatment

The cylindrical specimens having a length of 70 mm and a diameter of 10 mm were prepared to perform thermal cycling heat treatment (TCHT) on Gleeble® 3800. While performing TCHT, a k-type thermocouple was spot-welded at the middle of the specimen to record the live temperature of the steel specimen. The TCHT schedules for all the three sets of TCHT are shown in Fig. 1(a), (b) and (c) on program temperature (PTemp) and time graph. Due to the reduced cooling rate near the room temperature (RT), the actual temperature of the thermocouple varied with a slightly different rate as shown by the dotted lines in Fig. 1. This can be closely seen in the zoomed area of Fig. 1(a). A similar type of cooling occurred in

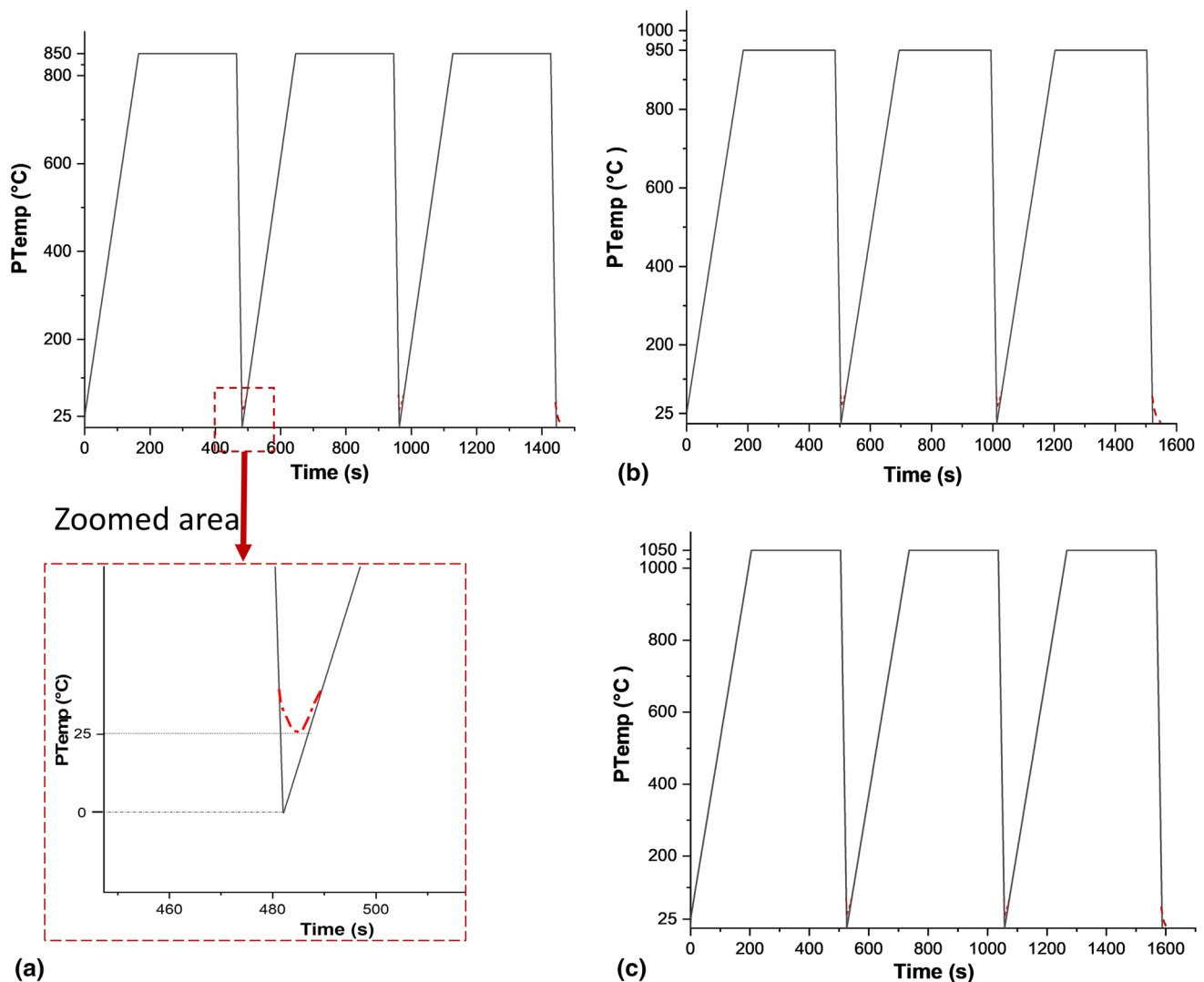


Fig. 1 Schematic diagram of cyclic heat treatment schedules for: (a) TCHT-850, (b) TCHT-950, and (c) TCHT-1050 specimens

Fig. 1(b) and (c). In each cycle of TCHT set, heating was done at a rate of 5 °C/s to a temperature (850, 950, and 1050 °C, respectively) and held for 5 min at this temperature. Then, a fast cooling of the specimens at a rate of 50 °C/s was done to bring the specimens to room temperature. The specimens were taken out from Gleeble after three cycles of each schedule. All the characterizations were performed after conducting three cycles. The TCHT performed at 850 °C is designated as TCHT-850, at 950 °C as TCHT-950, and at 1050 °C as TCHT-1050.

### 2.3 Microstructural Characterization

The phase transformation and the evolution of the microstructure of ASR and TCHT processed steel specimens were characterized by optical, x-ray analysis, SEM and TEM microscopy. Small specimens from the ASR billet and the TCHT processed specimens were cut for the characterization. To study the principal characteristics of thermal cycling heat treatment, specimens were cut from exactly the halfway of the specimen where the thermocouple was welded. These specimens were flattened by using belt grinding. Further, the specimens were polished with 320, 800, 1200, and 1500 grit size emery papers. The paper polishing was followed by cloth polishing with 0.5 μm diamond paste. Villela's reagent (having composition 1 g picric acid + 5 mL HCl + 100 mL ethanol) was applied to reveal the microstructure. A Lieca DMI 5000 M Light Optical Microscope (LOM) was used to take the digital images of microstructures. The scanning electron microscope (SEM), FEI QUANTA 200 FESEM, was also used to take the digital images of microstructures. For the TEM study, the thin film was jet polished by twinjet polisher in a solution of 10% HClO<sub>4</sub> + 90% ethanol. The TEM was performed on Jeol JEM-3200 FS high-resolution transmission electron microscope (HRTEM) to visualize the dislocations.

Both ASR and TCHT processed specimens were analyzed with x-ray diffraction. The x-ray diffraction (XRD) patterns were recorded by using Rigaku Smartlab x-ray diffractometer with CoK $\alpha$  radiation (wavelength ( $\lambda$ ) = 1.77 Å). The patterns were recorded for a 2 $\theta$  range of 30-120° at the rate of 2°/min and analyzed by using X'pertHighScore Plus software with PDF4 plugged in.

### 2.4 Mechanical Properties

The hardness of as-received (ASR) and TCHT processed specimens was measured on a FIE VM50 Vickers hardness tester. The tests were performed at 10 kg load with 15 s dwell time. The specimens were polished as per standard metallographic techniques before performing the tests. For each specimen (ASR and TCHT processed specimens), 10 readings

were taken and the average of the 10 readings along with the standard deviation is reported. The micro-hardness of individual phases in all specimens was measured by using a UHL VMHT micro-hardness tester with 50 g load and 15 s dwell time. For micro-hardness, five readings were taken for each phase and the average value along with standard deviation is reported. A gap of minimum 5 times the diameter of the indenter was maintained between any two indentations during both macro and micro-hardness measurements. The notched tensile tests were conducted at room temperature to study the tensile properties of the ASR and TCHT processed specimens. The notched tensile specimens were selected due to the limited length of the TCHT processed zone (zone of interest) of the TCHT processed specimen in Gleeble. The geometry of the notched tensile specimen is shown in Fig. 2 (Ref 23, 24). The total length of the specimen was 70 mm with 10 mm diameter. The length of the zone of interest was 10 mm. The minimum diameter in the notched area was 6 mm, and the radius of the notch was 3 mm. All tensile tests were performed on a Tinius Olsen H75KS tensile testing machine for both ASR and TCHT processed specimens. The cross-head speed in the tensile tests was kept 0.6 mm/min. Three samples for each condition were tested, and the average value is reported. In the notched tensile test, load versus extension data were recorded. Then, the calculations for UTS and ductility were done by measuring the diameter of the specimen after fracture and applying Eq 1, 2, 3, and 4 as mentioned in the text (Ref 25, 26). The digital images of the fractured surface of the tensile tested specimens were taken on FEI QUANTA 200 FESEM to analyze the mode of fracture.

## 3. Results

### 3.1 Microstructure Examination

Optical and SEM micrographs of the as-received and TCHT processed specimens are shown in Fig. 3 and 4, respectively. The optical micrograph of the as-received 13-4 MSS comprises the blocks of martensitic laths and the elongated colonies of delta-ferrite as shown in Fig. 3(a). The fraction of  $\delta$ -ferrite is small and indicated by arrows in Fig. 3(a). The packets of the lath martensite and ferrite phases can be closely examined in the SEM image in Fig. 4(a). The presence of a small amount of retained austenite in between the laths was observed from the SEM micrograph (Fig. 4a). This was neglected in the calculation of volume fractions of martensite and delta-ferrite. Further, it can also be observed that the size of packets and

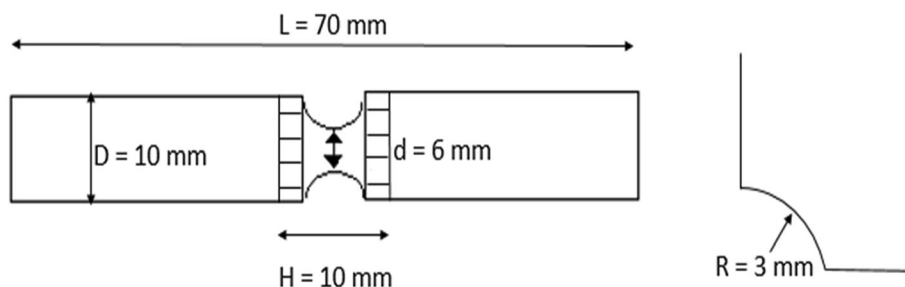
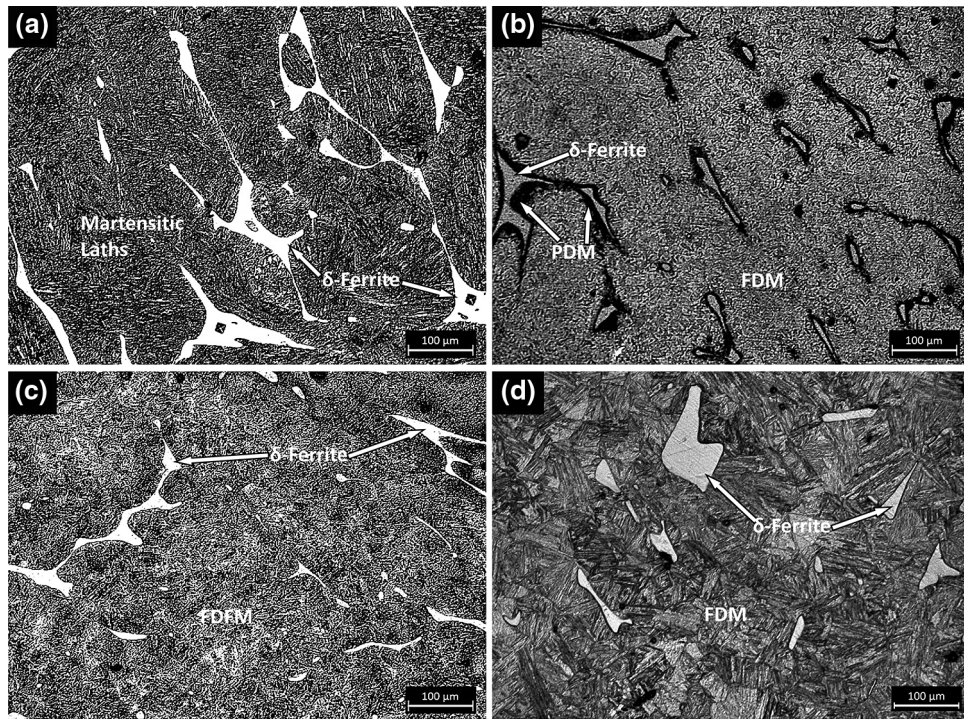
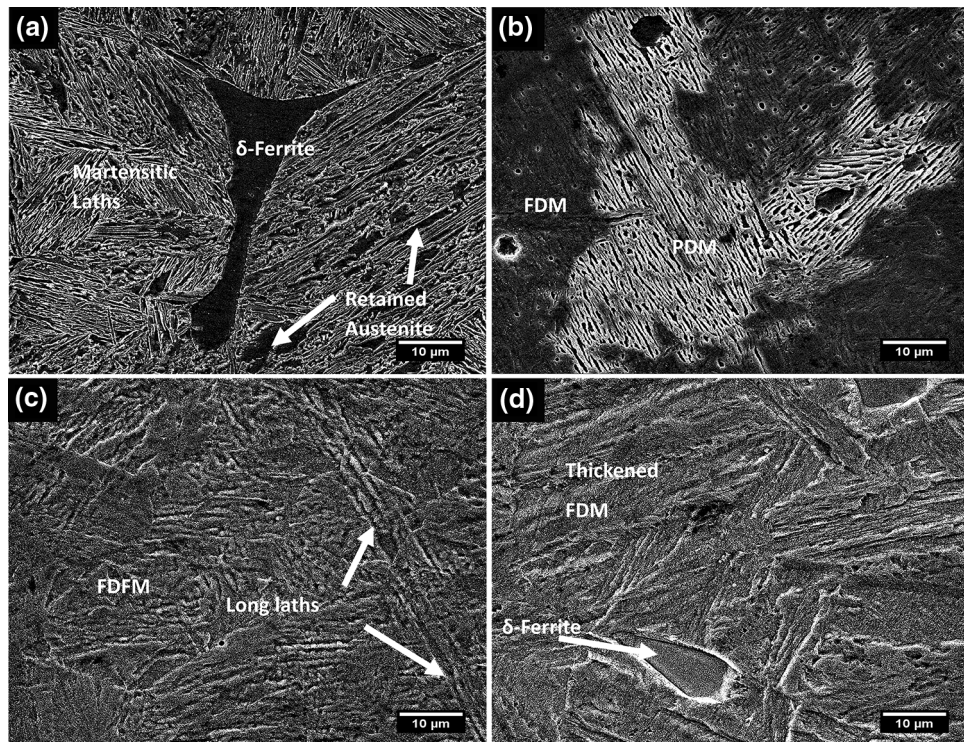


Fig. 2 Schematic geometry of the notched tensile specimen





**Fig. 3** Optical micrographs having lath martensite packets and  $\delta$ -ferritic features observed in: (a) 13-4 ASR, (b) TCHT-850, (c) TCHT-950, and (d) TCHT-1050 specimens



**Fig. 4** SEM images demonstrating the dissolution of martensite and the refinement of martensitic blocks along with the temperature of thermal cycling in: (a) 13-4 ASR, (b) TCHT-850, (c) TCHT-950, and (d) TCHT-1050 specimens

blocks is large. These blocks are containing the laths of martensite.

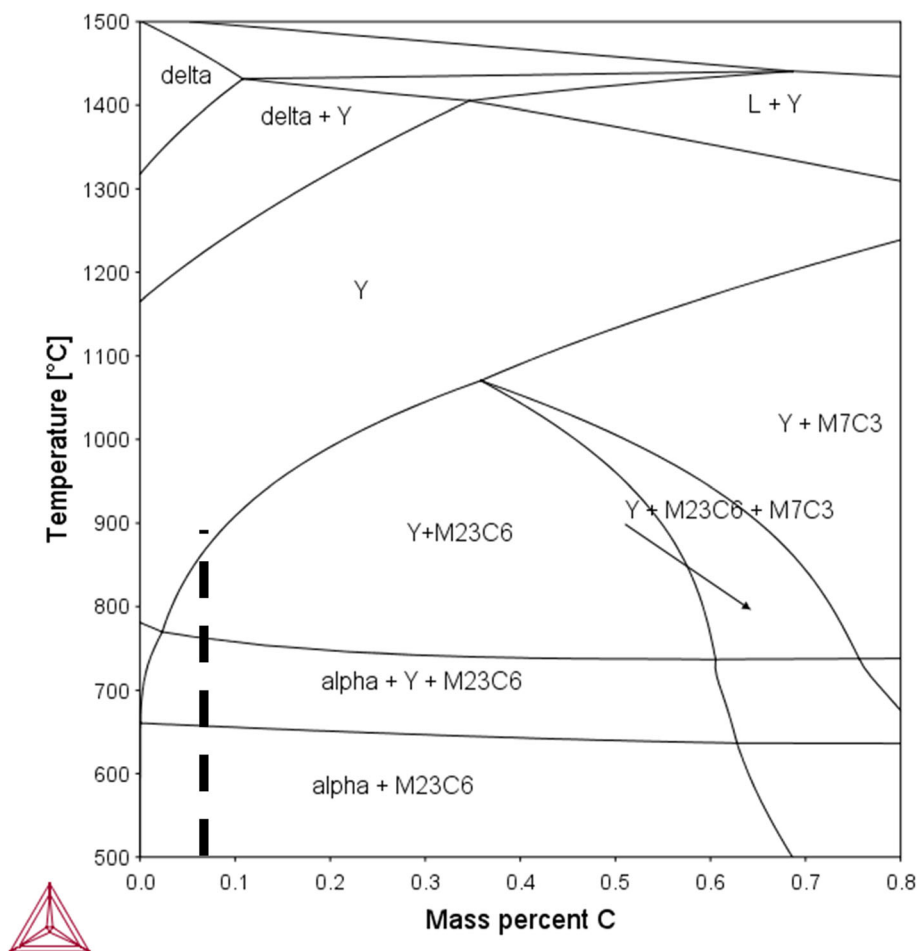
The volume fraction measurement indicated that delta-ferrite is 12.5% and of martensite is 87.5% and is shown in Table 1.

Both the volume fraction of delta-ferrite and the average size of delta-ferrite were determined by quantitative metallography (see Table 1). The present composition falls closer to the fully martensitic region in the Schaeffler diagram which verifies the



**Table 1** Variation of various microstructural features and the dislocation density of TCHT processed specimens

Features	Specimen code			
	13-4 ASR	TCHT-850	TCHT-950	TCHT-1050
Volume fraction of $\delta$ ferrite, %	12.5 $\pm$ 0.2	9.5 $\pm$ 0.7	6.3 $\pm$ 0.05	5.5 $\pm$ 0.37
Average grain size of $\delta$ ferrite, mean $\pm$ SD, $\mu\text{m}$	25.10 $\pm$ 6.0	23.3 $\pm$ 3.16	22.32 $\pm$ 0.14	20.98 $\pm$ 5.06
Block size, mean $\pm$ SD, $\mu\text{m}$	29.5 $\pm$ 8.5	...	22.3 $\pm$ 4.5	16.7 $\pm$ 1.6
Dislocation density, $10^{15} \text{ m}^{-2}$	2.246	3.953	4.423	4.248

**Fig. 5** Calculated phase diagram for the present steel by using Thermo-Calc<sup>®</sup> software (in Figure, Y denotes FCC austenite phase, while L denotes liquid phase)

fraction of phases present in Fig. 3(a) and 4(a). A similar microstructure was observed in (Ref 1, 27) for the as-received 13-4 MSS.

The microstructure evolution due to TCHT at 850 °C for three cycles is shown in Fig. 3(b) and 4(b). The optical micrograph (Fig. 3b) indicates the presence of three regions in the microstructure, fully dissolved martensite (FDM), partially dissolved martensite (PDM), and slightly fragmented ferrite. The PDM can be closely observed by the SEM image (Fig. 4b). The packets of lath martensite (as in 13-4 ASR) got refined due to TCHT which are designated as FDM in Fig. 3(b) and 4(b). The FDM contributes almost 85% in the TCHT-850 microstructure. Being in the dominating amount, the FDM influences the mechanical properties significantly for TCHT-850.

The calculated phase diagram for the present steel by using Thermo-Calc<sup>®</sup> software is shown in Fig. 5. It can be seen from Fig. 5 that the transformations of this steel start above 850 °C. So, some fraction remained partially undissolved during TCHT at 850 °C and formed PDM. The short duration (5 min) holding during TCHT is the other reason behind the formation of PDM. The fraction of PDM is very small and formed adjacent to the boundaries of ferrite. The PDM is having different mechanical properties (discussed in the coming subsection) than FDM and ferrite, but its influence on the bulk properties is negligible. This is due to the presence of its small amount. The volume fraction of delta-ferrite is slightly reduced (from 12.5 to 9.5%) due to TCHT at 850 °C as compared to the delta-ferrite of 13-4 ASR steel. The volume fractions of delta-

ferrite (9.5%) and the average grain size of delta ferrite (23.3  $\mu\text{m}$ ) are stated in Table 1.

The microstructure evolution due to TCHT at 950 °C for three cycles is shown in Fig. 3(c) and 4(c). The optical micrograph (Fig. 3c) indicates the presence of two regions in the microstructure, fully dissolved fine martensite (FDFM), and slightly fragmented ferrite. The TCHT temperature of this schedule (i.e., 950 °C) lies in the austenization region as verified by the calculated phase diagram of the present composition in Thermo-Calc<sup>®</sup> software (Fig. 5). So, the packets of lath martensite got refined to a larger extent and possess a more refined lath morphology. The refined lath morphology in TCHT-950 steel is designated as FDFM as shown in Fig. 3(c) and 4(c). The FDFM comprises more uniformly distributed and closely packed martensitic laths as compared to other specimens. Figure 4(c) shows the SEM image of FDFM. From the SEM image, it can be observed that some blocks contain long martensitic laths along with the blocks and packets having fragmented martensitic laths. This condition may also be studied in an analogy to bimodal lath structure where fragmented laths exist along with long laths. The bimodal structure has been proven to have better mechanical properties than normal unimodal structure (Ref 28). Further, it can also be noted that no fraction of the PDM phase is observed in the TCHT-950. The fraction of martensitic content in the microstructure, i.e., FDFM rose up to almost 94% due to TCHT at 950 °C. So, the bulk properties can be approximated with the properties of FDFM. Delta-ferrite in the case of TCHT-950 decreased to 6.3% and remained almost 50%, and 30% lesser than the corresponding phase of 13-4 ASR, and TCHT-850 steel (as in Table 1), respectively. Due to its deleterious effect on hardness, delta-ferrite is not desired, while martensite (here FDFM) is a desirable phase because of its high hardness. So, the reduction in undesirable  $\delta$ -ferrite phase and evolution of FDFM is a major achievement of this TCHT schedule.

The microstructure evolution due to TCHT at 1050 °C for three cycles is shown in Fig. 3(d) and 4(d). The optical micrograph (Fig. 3d) indicates the presence of two regions in the microstructure, fully dissolved martensite (FDM), and fragmented ferrite. At the higher temperatures (1050 °C), grain coarsening occurs through the movement of grain boundaries (Ref 29). Although the refinement of blocks occurred, the laths inside fragmented blocks got thickened. So, the laths in FDM phase of TCHT-1050 are present in slightly coarser form as compared to other specimens studied in the present research. The thickened laths and refined blocks can also be viewed from the SEM micrograph, i.e., Figure 4(d). The other reason behind this may be the cooling from higher temperature (1050 °C) as can be interpreted from the continuous cooling transformation diagram (CCT) (Ref 30). Moreover, the FDM is non-uniformly distributed as can be seen in Fig. 3(d). The FDM in TCHT-1050 contributes 94.5% in the microstructure. The amount of  $\delta$ -ferrite phase is more or less of the same order as in the case of TCHT-950 steel but is 56%, and 42% lesser than the corresponding phase of 13-4 ASR and TCHT-850 steel (as in Table 1), respectively. The average grain size of the ferrite declined slightly as can be seen from Table 1.

The XRD analysis also verifies the presence of different phases for both as-received and TCHT processed specimens. Figure 6(a), (b), (c) and (d) shows the x-ray diffractograms. The XRD pattern for the as-received (13-4 ASR) specimen, shown in Fig. 6(a), indicates the presence of ferrite (BCC) and

martensite (BCT) and austenite (FCC) which verifies the presence of  $\delta$ -ferrite phase, martensitic phase, and retained austenite phase, respectively. The lower intensities of all the peaks of austenite confirm a negligible amount of retained austenite phase in the 13-4 ASR. A small fraction of retained austenite was also observed in the concerned SEM micrograph. Due to the low carbon content in the present steel, the BCT structure of martensite approached the BCC structure (BCT  $\approx$  BCC). Hence, most of the peaks for ferrite and martensite overlap in XRD patterns. Similar peaks for 13-4 MSS, except the austenite peaks, have also been observed by other researchers (Ref 27).

In XRD patterns of TCHT-850 specimen, the austenite peaks have disappeared due to TCHT as shown in Fig. 6(b) which indicates that the TCHT-850 specimen does not contain the retained austenitic (FCC) phase. The peaks of martensite indicate the presence of BCT martensitic phase, while the peaks of the ferrite phase indicate the presence of BCC  $\delta$ -ferrite phase in TCHT-850 and other specimens. Figure 6(c) shows the selected XRD peaks for TCHT-950 and Fig. 6(d) for TCHT-1050.

The intensities of the  $\delta$ -ferrite peaks are getting reduced due to TCHT from TCHT-850 onwards indicating the reduction in the amount of  $\delta$ -ferrite in TCHT-850, TCHT-950, and TCHT-1050. The ferritic peaks of (211) from TCHT-950, and (310) from TCHT-950 and TCHT-1050 got disappeared. The overlapping of ferrite and martensite peaks takes place for all the TCHT processed specimens.

## 3.2 Mechanical Properties

**3.2.1 Hardness.** The results of micro-hardness for the individual phases present in the various specimens and the bulk material macro-hardness are shown in Fig. 7. The as-received 13-4 MSS possesses the lowest hardness (274 HV) due to the coarse martensite and relatively higher volume fraction of soft delta ferrite. The presence of retained austenite also decreases the hardness (Ref 31). Being the major constituent, martensite is largely responsible for the bulk hardness in all the specimens. The micro-hardness of the martensite phase (331 HV) is also the lowest in 13-4 ASR. This is due to the coarser martensite which causes a reduction in hardness (Ref 32).

The TCHT increased both micro- and macro-hardness for all the TCHT processed specimens. A substantial rise in the micro-hardness of the martensitic phase (411 HV) and the bulk hardness (382 HV) was observed for TCHT-850 specimen. This is due to the martensitic refinement through the TCHT and the formation of FDM. In TCHT-850 specimen, the PDM phase adjacent to the  $\delta$ -ferrite phase was also observed which is having slightly lower micro-hardness (356 HV) than FDM martensite. This may also be responsible for lowering the bulk hardness of TCHT-850, but the amount is so less that the effects on bulk hardness are negligible. By increasing the TCHT temperature (i.e., 950 °C), the refinement in the martensitic laths accelerated and the formation of FDFM took place. This resulted in higher micro-hardness (429 HV) and bulk hardness (413 HV) of TCHT-950. The decrease in the soft delta-ferrite fraction in TCHT-950 is also responsible for this rise in hardness along with the martensitic refinement and formation of FDFM. An increase in micro-hardness of the delta-ferrite phase (243 HV) for TCHT-950 was also observed as compared to the delta-ferrite phase (230 HV) of TCHT-850. The micro-hardness of martensite in TCHT-1050 specimen increased in a similar

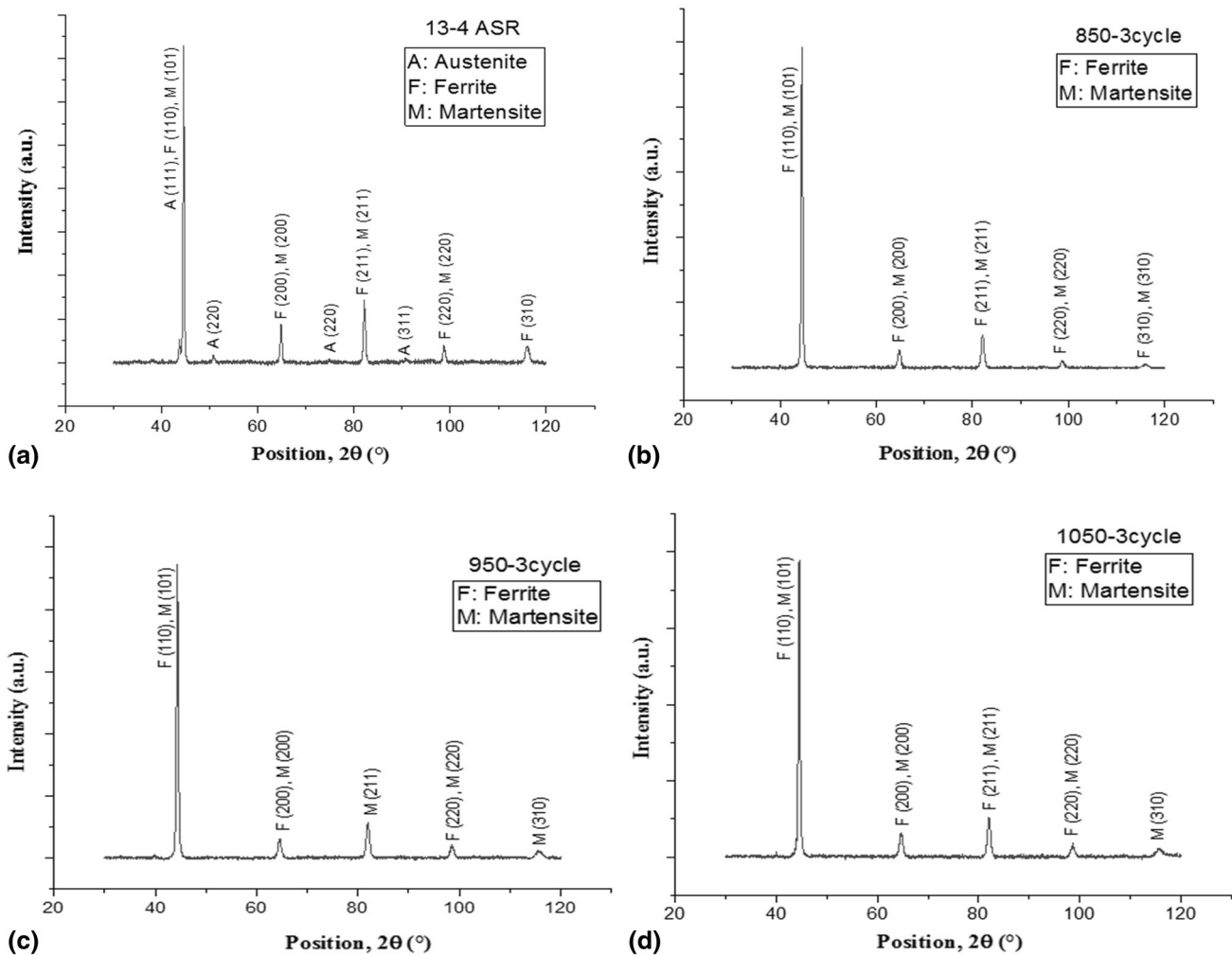


**Fig. 6** X-ray diffractograms for as-received and TCHT processed specimens: (a) 13-4 ASR, (b) TCHT-850, (c) TCHT-950, and (d) TCHT-1050 specimens

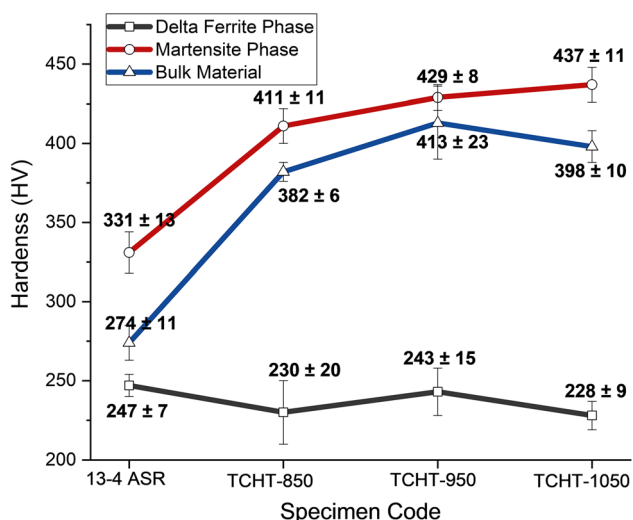


**Fig. 7** Variation of micro- and macro-hardness with TCHT temperature in the as-received and TCHT processed specimens

fashion (437 HV) and attained the highest value among all the specimens. But the bulk hardness (398 HV) declined slightly as compared to TCHT-950 specimen.

The micro-hardness of the martensitic phase for all the TCHT specimens increased due to the refinement of the martensite blocks. This increased with the temperature of the TCHT schedule, but the rate of increase declined. A 24% hike in micro-hardness of martensite is observed in TCHT-850 than the counterpart of 13-4 ASR (Fig. 7). This hike is increased to 32% in the case of TCHT-1050. The bulk hardness is a function of micro-hardness of its dominant phase (i.e., martensite), and the amounts of retained austenite and delta-ferrite present in it. The hardness increased for all TCHT processed specimens as compared to 13-4 ASR specimen because the retained austenite was not observed in TCHT processed specimens. The highest bulk hardness with a hike of 50% was observed in TCHT-950. The hardness results obtained in this study are well above the results obtained in the other studies [343 HV (Ref 33) and 386 HV (Ref 34)] in the literature.

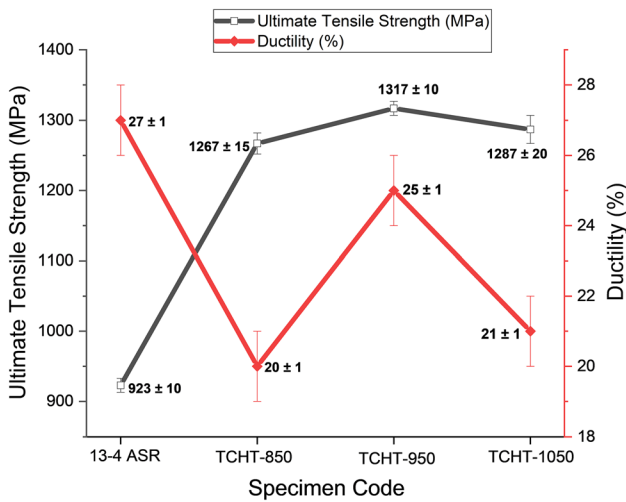


**Fig. 8** Variation of tensile properties (ultimate tensile stress (UTS), and ductility) in various specimens due to cyclic thermal treatment

**3.2.2 Tensile Properties.** The normalized tensile properties for all the specimens are presented in Fig. 8. It is important to note that the tensile properties presented here are converted from notched tensile properties obtained through the notched tensile test. The shape correction factor ( $G$ ) was utilized to convert the notched tensile properties to engineering tensile properties according to the Eq 1, 2, 3, and 4 as in (Ref 25, 26). In these equations,  $\epsilon_{\text{True}}$  is logarithmic strain,  $\epsilon_{\text{Engg}}$  is engineering strain,  $R$ ,  $d$  and  $d_f$  are notch radius, initial diameter in notch and diameter after fracture, respectively (Fig. 2), and  $\epsilon_{\text{max}}$  is logarithmic strain at maximum load. The  $\sigma_n$  and  $\sigma_{\text{un}}$  are notched and un-notched tensile strengths, respectively. The properties obtained are different from the un-notched tensile test engineering stress and engineering strain and may bear an error of 5-10% (Ref 35).

$$\epsilon_{\text{True}} = 2 \ln \left( \frac{d}{d_f} \right) \quad (\text{Eq 1})$$

$$\epsilon_{\text{True}} = \ln(1 + \epsilon_{\text{Engg}}) \quad (\text{Eq 2})$$

$$G = \left[ 1.007 + 0.18777 \left( \frac{d}{R} \right) - 0.01313 \left( \frac{d}{R} \right)^2 \right] (1.053 - 0.53 \epsilon_{\text{max}}) \quad (\text{Eq 3})$$

$$\sigma_{\text{un}} = \frac{\sigma_n}{G} \quad (\text{Eq 4})$$

The as-received specimen (13-4 ASR) possesses the least UTS (923 MPa) and a moderate ductility (27%). The presence of soft delta-ferrite and the coarser martensite are responsible for its high ductility and low UTS. In TCHT processed specimens, the UTS increased significantly with a small decrease in ductility. The UTS results follow a similar trend as the bulk hardness. Most of the heat treatments increase the strength properties at the expense of ductility (Ref 36). But this cycling treatment enhanced the strength properties without a significant decrease in ductility. The TCHT-850 specimen attained a higher UTS (1267 MPa) and slightly lesser ductility (20%) than the counterpart of 13-4 ASR.

In TCHT-950, the highest UTS (1317 MPa) and ductility (25%) were observed as compared to the counterpart of TCHT-850. This could be due to the absence of PDM in TCHT-950. In addition to this, the absence of retained austenite and reduced fraction of  $\delta$ -ferrite phase also contributed to the increased UTS. Moreover, the FDM (almost 95%) is present as FDFM (in a more refined state than earlier cases) which is harder as per the Hall-Petch strengthening relation.

A moderate ductility (21%) and higher UTS (1287 MPa) were observed for the TCHT-1050 steel. This is due to the presence of slightly coarser FDM. The coarse martensite offers a lower hindrance to the dislocation motion (Ref 37). TCHT-950 possesses the highest UTS which is 42% higher than the counterpart of 13-4 ASR. It shows a 2% reduction in ductility than the counterpart of 13-4 ASR. TCHT-1050 possesses a 39% hike in UTS (1287 MPa) and a 22% decline in ductility (21%) than the counterparts of 13-4 ASR. The combination of UTS and ductility (1317 MPa, and 25%) is better than the other studies [1015 MPa and 26% (Ref 27), 1018 MPa and 20% (Ref 33), 1103 MPa and 13% (Ref 34), and 840 MPa and 22.6% (Ref 38)] reported in the literature.

**3.2.3 Fractography.** The fractographs of the notched tensile tested specimens are shown in FESEM micrographs in Fig. 9(a), (b), (c) and (d). The fractograph of the as-received (13-4 ASR) (as shown in Fig. 9a) demonstrates a mixed-mode of fracture and exhibits dimples in the major region indicating a ductile fracture. The dimples are irregular in size and shape. A minor region of the fractograph also exhibits cleavage facets which favor brittle fracture. The ductile fracture features (i.e., dimples) in the martensitic laths region dominated the fracture mechanism of the steel. It can be observed from Fig. 9(a) that the dimples are large in number but smaller in size when compared to the fractographs of other specimens. Large dimples are developed by the coalescence of micro-voids in the martensitic region of the specimen. Due to the increased load, the coalescence of micro-voids takes place and the cavities get enlarged and undergo a large plastic deformation to form large dimples. The size of dimples can be taken as a measure of ductility (Ref 39). The fracture features of the fractograph explain the ductility of the ASR steel and verify the results of a good ductility of 27% as discussed earlier.

The FESEM fractograph of the specimen subjected to TCHT at 850 °C, i.e., TCHT-850 steel, is shown in Fig. 9(b) which exhibits cleavage facets along with some irregular-sized dimples. In this steel, cleavage fracture might have occurred in the FDM region and dimples in PDM and delta ferrite regions. As can be seen from the fractograph, the cleavage facets fracture dominated for this specimen. This is characterized by a somewhat brittle fracture. The fracture morphology favors the decreased ductility (20%) which is 26% lower than the 13-4 ASR specimen.

The FESEM fractograph of the specimen subjected to TCHT at 950 °C, i.e., TCHT-950 steel, is shown in Fig. 9(c) which exhibits large and irregular shape and size dimples in the major region along with some cleavage facets. The dimples generated in this specimen are lesser in number but bigger in size as compared to 13-4 ASR specimen. This can be characterized for superior ductility which is 25% higher than TCHT-850. The evolved bimodal lath structure and raised fraction of uniformly distributed martensite as refined FDM (almost 95%) caused the fracture with significant plastic deformation.



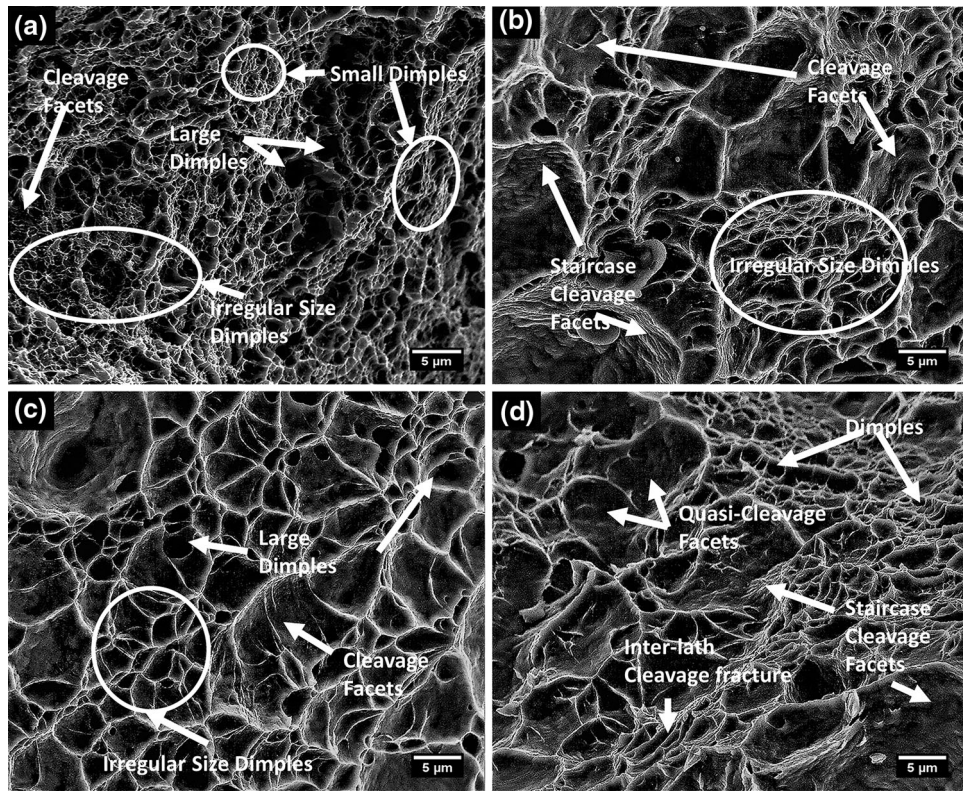


**Fig. 9** SEM fractographs of notched tensile tested specimens observed in: (a) 13-4 ASR, (b) TCHT-850, (c) TCHT-950, and (d) TCHT-1050 specimens

The FESEM fractograph of the specimen subjected to TCHT at 1050 °C, i.e., TCHT-1050 steel, is shown in Fig. 9(d) which exhibits cleavage facets (river-like pattern) and staircase cleavage facets. The fractograph also reveals a few irregularly shaped dimples. The cleavage facets are characterized by brittle fracture. A mixed mode of fracture mechanism can be witnessed in Fig. 9(d). The cleavage facets are the dominating features in this specimen, thereby causing somewhat brittle fracture as compared to 13-4 ASR and TCHT-950 specimens. The concerned fractograph verifies the reduced ductility results (21%) for this steel.

### 3.3 Block Size Analysis

The present thermal cyclic heat treatment improved the mechanical properties significantly. The substantial enhancement in hardness and UTS for TCHT-950 and a slight decline in hardness and UTS for TCHT 1050 directed us to further investigate the mechanism at the block level. The blocks were identified based on the misorientation angle smaller than  $10.53^\circ$  (Ref 40) and drawn on a separate sheet. The FESEM images for 13-4 ASR, TCHT-950, and TCHT-1050 and their corresponding blocks are shown in Fig. 10(a), (b), (c), (d), (e) and (f). The block boundaries were drawn manually and may bear some errors. The refinement in the blocks was verified by visual inspection of Fig. 10. The block sizes calculated by using quantitative metallurgy are stated in Table 1.

As stated earlier, the prior austenite grain size (PAGS) strongly controls the mechanical properties of the steels (Ref 2). In the case of lath martensite, the microstructure is composed of three-level hierarchy—packets, blocks, and laths (Ref 41).

Many studies postulated that the sizes of packets and blocks are linearly dependent on the size of PAGS (Ref 42). Also, the block size is considered equivalent to grain size (Ref 41, 42). From this, it can be concluded that the block size controls the mechanical properties significantly. The average block size was plotted against the temperature of TCHT and mechanical properties (hardness, and UTS) to further investigate the correlation between block size and mechanical properties. Figure 11 shows the relations of block size, hardness, and UTS to the temperature of thermal cycling. Firstly, it can be observed that the block size decreases as the temperature of thermal cycling increases. As the temperature is the only variable among TCHT schedules, the temperature increment is stated here. Secondly, hardness and UTS vary in a similar trend which first increases and then decreases slightly as the temperature increases. The average block size decreases continuously.

### 3.4 Dislocation Density

The dislocations significantly influence the mechanical properties. So, the quantification of the dislocation density was performed for a better understanding. Dislocation densities calculated from XRD results for as-received and TCHT-processed specimens are shown in Table 1. The grain size was calculated by Scherrer's relation (Ref 43), and the dislocation density was calculated by using the Williamson–Smallman equation (Ref 44). From Table 1, it can be seen that the dislocation density increased in a rapid way for the processed specimens. The dislocation density became almost double in the case of TCHT-950 ( $4.423 \times 10^{15} \text{ m}^{-2}$ ) than in 13-4 ASR ( $2.246 \times 10^{15} \text{ m}^{-2}$ ). A small decrease in dislocation

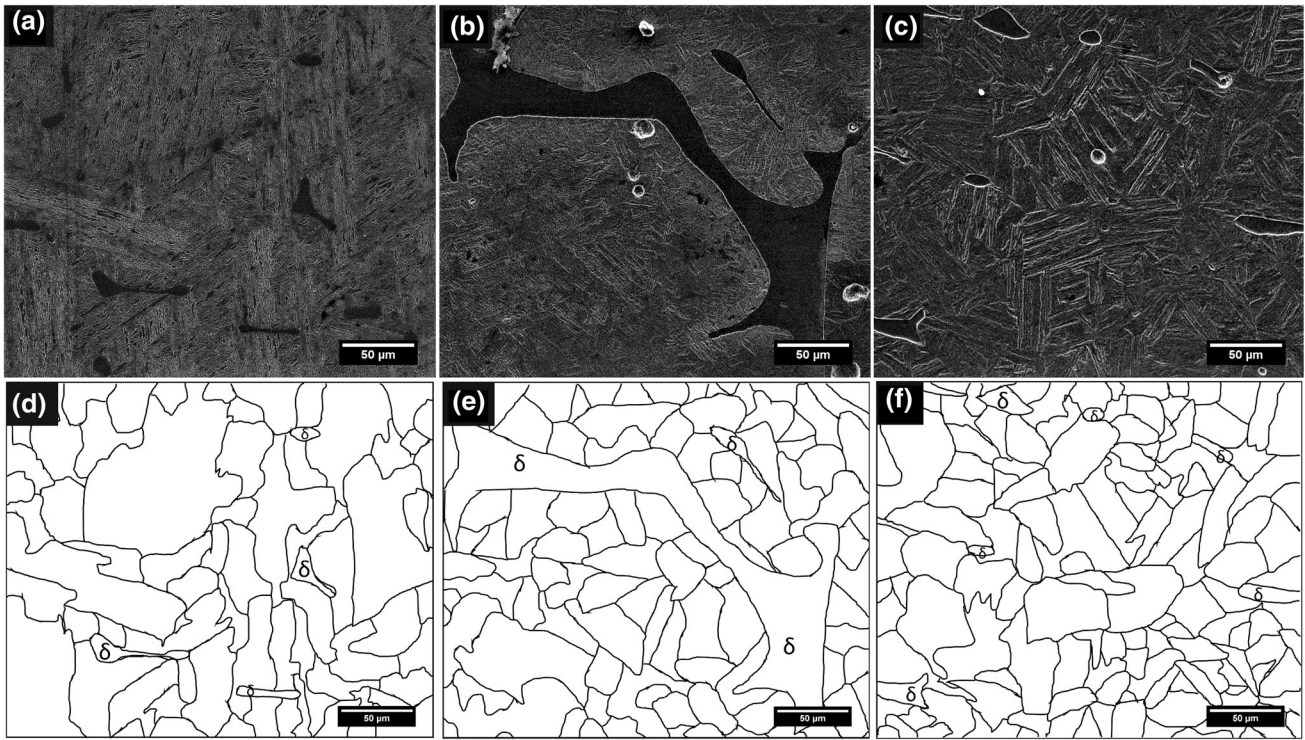


**Fig. 10** Drawn block boundaries illustrating the refinement due to cyclic thermal treatment observed in: (a) FESEM image of 13-4 ASR, (b) FESEM image of TCHT-950, (c) FESEM image of TCHT-1050, (d) block boundaries of 13-4 ASR, (e) block boundaries of TCHT-950, and (f) block boundaries of TCHT-1050 specimens

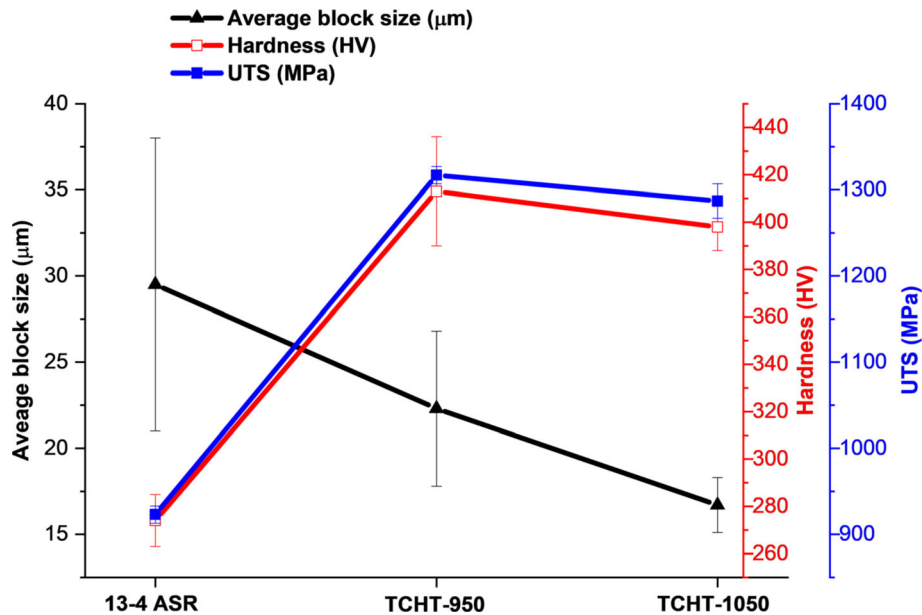


**Fig. 11** The variations of hardness, UTS, and block size along with the temperature of cyclic treatment in 13-4 ASR, TCHT-950, and TCHT-1050 specimens

density was also observed in the case of TCHT-1050 ( $4.248 \times 10^{15} \text{ m}^{-2}$ ) as compared to the counterpart of TCHT-950.

The attempt was also made to visualize the dislocation density through transmission electron microscopy. The bright-field (BF) transmission electron micrographs are shown in Fig. 12. The dotted white lines indicate the martensite laths.

The symbol of triangle depicts the dislocation region on the micrograph. The TEM micrograph for 13-4 ASR is shown in Fig. 12(a) which illustrates the dislocations in the lath martensite structure. Figure 12(b) shows the BF TEM micrographs for TCHT-1050 specimen which reveals that the fully dissolved martensite (FDM) of TCHT-1050 specimen consists of highly dislocated regions in the micrograph. The TEM micrographs



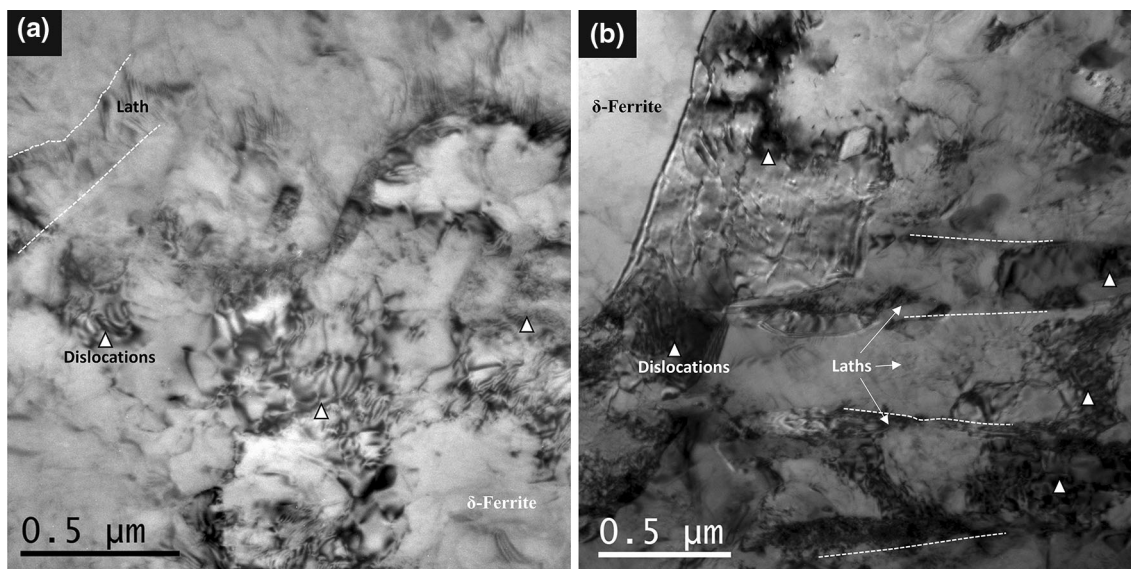


**Fig. 12** Bright-field TEM micrographs of (a) 13-4 ASR, and (b) TCHT-1050 specimens

are in good agreement with the results of calculated dislocation densities.

#### 4. Discussion

The martensite structure can be strengthened by the following five mechanisms: (1) carbide precipitation strengthening (Ref 42), (2) solid solution strengthening (Ref 45), (3) high-angle boundary hardening (Ref 41), (4) increase in dislocation density (Ref 46), and (5) microstructure (Ref 47). The present study is based on the microstructural strengthening and the strengthening due to the increase in the dislocation density of the lath martensite.

Generally, hardness is a function of carbon content in the material but for a fix carbon content, and the hardness can be varied by controlling the microstructure and the dislocation density. The microstructural parameters which influence the hardness are: (1) amount of delta-ferrite (Ref 47), (2) amount of retained austenite (Ref 48, 49), (3) block size (Ref 32, 41), (4) amount of martensitic content (Ref 47), and (5) lath size (Ref 50). Delta ferrite absorbs very less amount of carbon due to lesser carbon solubility in delta ferrite (Ref 47). So, delta ferrite is soft and ductile and its amount decreases the bulk hardness. Due to its deleterious effect, delta-ferrite is not desired. The amount of retained austenite deteriorates the hardness due to the following two reasons: (1) retained austenite itself is soft and tough and (2) it removes the carbon atoms from the martensite because of its higher solubility and softens the martensite matrix (Ref 51). The block size is considered equivalent to the conventional grain size (Ref 41), and the block boundaries hinder the motion of dislocation (Ref 52). While taking the hardness, the motion of dislocations occurs to deform the material. So, the lesser the block size, the more the block boundaries and the more the hindrance to the motion of dislocation and hence the more the hardness. The martensite phase consists of hard martensitic laths and hence a desired phase. The carbon atoms present in the martensite phase segregate on the lath boundaries which increase the dislocation

density (Ref 53). The lath size is generally explained by the width of the lath. As stated earlier, the segregated carbon atoms on the lath boundaries increase the dislocation density. The dislocation density varies almost inversely with the lath size (width) (Ref 37). So, the larger the lath size, the lesser the dislocation density and hence the lesser the hardness/strength.

All these microstructural parameters and dislocation density can be controlled by the processing conditions. The present cyclic thermal treatment varied these microstructural parameters and dislocation density in an appropriate fashion. The base material (13-4 ASR) consists of relatively higher amounts of delta-ferrite, retained austenite, and hence a lesser amount of martensite as can be seen from Fig. 3, 4, and Table 1. The block size is largest as can be observed from Fig. 10 and Table 1. So, the hardness and micro-hardness are lesser than the TCHT processed steels. The retained austenite diminished and delta ferrite deteriorated in all the processed specimens which consequently increased the martensitic content in the steel. The refinement in the block size can be verified by Fig. 10 and Table 1. The first four parameters favored the increase in hardness in all the TCHT processed specimens. From Fig. 7 and 11, it can be observed that the hardness increases up to 950 °C (i.e., TCHT-950) and then decreases slightly for TCHT-1050. In this slight decrement for TCHT-1050, the fifth parameter (i.e., lath size) might have played a dominant role. It can be visually inspected from Fig. 4 and 10 that there is no significant difference in lath sizes for TCHT-850 and TCHT-950. But the lath sizes for TCHT-1050 is much coarser than other conditions. This statement is based on visual inspection of FESEM images only. The quantitative assessment of lath sizes was not done in this study. More carbon atoms segregated on the lath boundaries probably due to the refinement of laths and consequently higher dislocations might have accumulated in TCHT processed specimens. The coarser laths in TCHT-1050 have decreased the dislocation density slightly. The strength-lath size correlation is in good agreement with other studies (Ref 50). However, some studies did not observe this behavior (Ref 42). The calculated dislocation density (Table 1) and the visual inspection of highly dislocated TEM micrographs



(Fig. 12) also favored the results of hardness and tensile properties.

The microstructural parameters discussed for hardness influenced the ultimate tensile strength (UTS) in a similar fashion. Previous studies have agreed on the fact that the block boundaries act equivalent to grain boundaries in the Hall–Petch strengthening relation (Ref 41, 42, 52). This relation is verified for UTS in the present study. Moreover, the amounts of retained austenite, delta-ferrite, and the martensitic content supported the obtained results. Similar to the hardness, the lath size comes into the picture for deteriorating the UTS of TCHT-1050 slightly. All the five microstructural parameters supported the results which can be observed from Fig. 4, 10, and Table 1.

The ductility of the present steel depends on the amounts of retained austenite and delta-ferrite, block size, and laths size but in reverse fashion than hardness and UTS. The amount of delta-ferrite has more control on the ductility (Ref 47) than the other parameters. This is due to the fact that delta-ferrite deforms prior to the martensite matrix while accommodating the induced strain due to applied stress (Ref 54). This helps the larger plastic deformation of the bulk material and thereby increases the ductility. In the present study, the amount of delta-ferrite decreased from 12.5% (for 13-4 ASR) to 5.5% (for TCHT-1050) as the temperature of cycling increased (see Table 1). So, 13-4 ASR possesses a higher ductility than TCHT processed specimens as can be observed from Fig. 8. The bimodal lath structure and larger block size probably attributed to the increased ductility of TCHT-950 than other TCHT processed specimens. Due to the higher ductility of the 13-4 ASR, the fractograph (Fig. 9a) consists of dimples on the major area. The fractographs of TCHT processed specimens (Fig. 9b, c and d) consist of a mixed-mode of fracture.

## 5. Conclusions

The thermal cycling heat treatment (TCHT) was performed on 13%Cr-4%Ni martensitic stainless steel at three different temperatures (viz. 850, 950, and 1050 °C) for three cycles on Gleeble® 3800 and the following conclusions are made:

- The cyclic treatment possessed a fraction of undissolved martensite as PDM in TCHT-850 specimen. A bimodal lath structure was observed in TCHT-950. While performing TCHT at the higher temperature (1050 °C), the coarsening of laths occurred in TCHT-1050 specimen.
- XRD spectra demonstrated the overlapped peaks of delta-ferrite and martensite due to the low carbon content in the present steel. The reduced intensities of the peaks indicated a decrease in the amount of delta-ferrite for the TCHT processed specimens.
- The martensite blocks got refined from 29.5 μm (for 13-4 ASR) to 16.7 μm (for TCHT-1050), and the fraction of delta ferrite reduced from 12.5% (13-4 ASR) to 5.5% (TCHT-1050). The dislocation density increased substantially for the processed specimens. These factors were found to influence the mechanical properties of the specimens.
- The martensitic phase of TCHT-1050 specimen possessed the highest micro-hardness (437 HV). The bulk hardness was highest for TCHT-950 (413 HV). The highest UTS of 1317 MPa and ductility of 25% were achieved by TCHT-

950. The TCHT-950 specimen obtained the best combination of UTS, hardness, and ductility among all the specimens.

- This cyclic treatment (TCHT) is found to be a better route to improve the mechanical properties (UTS, hardness, and ductility) than the other methods addressed in the literature.

## References

1. G. Prakash and S.K. Nath, Studies on Enhancement of Silt Erosion Resistance of 13/4 Martensitic Stainless Steel by Low-Temperature Salt Bath Nitriding, *J. Mater. Eng. Perform.*, 2018, **27**(7), p 3206–3216
2. K. Nakazawa, Y. Kawabe, and S. Muneki, Grain Refinement of High-Strength Maraging Steels Through Cyclic Heat Treatment, *Mater. Sci. Eng.*, 1978, **33**(1), p 49–56
3. B.R. Kumar, S. Sharma, B.P. Kashyap, and N. Prabhu, Ultrafine Grained Microstructure Tailoring in Austenitic Stainless Steel for Enhanced Plasticity, *Mater. Des.*, 2015, **68**, p 63–71
4. J.N. Wang, J. Yang, Q. Xia, and Y. Wang, On the Grain Size Refinement of TiAl Alloys by Cyclic Heat Treatment, *Mater. Sci. Eng., A*, 2002, **329–331**, p 118–123
5. P. Payson, W.L. Hodapp, and J. Leeder, The Spheroidizing of Steel by Isothermal Transformation, *Trans. Am. Soc. Met.*, 1940, **28**, p 306
6. A. Mishra, C. Mondal, and J. Maity, Microstructural Modifications in AISI, 1080 Eutectoid Steel Under Combined Cyclic Heat Treatment, *Steel Res. Int.*, 2016, **87**(4), p 424–435
7. A. Mishra and J. Maity, Structure-Property Correlation of AISI, 1080 Steel Subjected to Cyclic Quenching Treatment, *Mater. Sci. Eng., A*, 2015, **646**, p 169–181
8. S. Mishra, A. Mishra, B.K. Show, and J. Maity, Simultaneous Enhancement of Ductility and Strength in AISI, 1080 Steel Through a Typical Cyclic Heat Treatment, *Mater. Sci. Eng., A*, 2017, **688**, p 262–271
9. S. Maji, A.R. Subhani, B.K. Show, and J. Maity, Effect of Cooling Rate on Microstructure and Mechanical Properties of Eutectoid Steel Under Cyclic Heat Treatment, *J. Mater. Eng. Perform.*, 2017, **26**, p 3058–3070
10. Z.Q. Lv, B. Wang, Z.H. Wang, S.H. Sun, and W.T. Fu, Effect of Cyclic Heat Treatments on Spheroidizing Behavior of Cementite in High Carbon Steel, *Mater. Sci. Eng., A*, 2013, **574**, p 143–148
11. A. Mishra, A. Saha, and J. Maity, Development of High Strength Ductile Eutectoid Steel Through Cyclic Heat Treatment Involving Incomplete Austenitization Followed by Forced Air Cooling, *Mater. Charact.*, 2016, **114**, p 277–288
12. A. Mishra, C. Mondal, and J. Maity, Effect of Combined Cyclic Heat Treatment on AISI, 1080 Steel: Part II-Mechanical Property Evaluation, *Steel Res. Int.*, 2017, **88**, p 1–10
13. Z.-Q. Lü, H.-F. Zhang, Q. Meng, Z.-H. Wang, and W.-T. Fu, Effect of Cyclic Annealing on Microstructure and Mechanical Properties of Medium Carbon Steel, *J. Iron. Steel Res. Int.*, 2016, **23**(2), p 145–150
14. A. Saha, D.K. Mondal, K. Biswas, and J. Maity, Microstructural Modifications and Changes in Mechanical Properties During Cyclic Heat Treatment of 0.16% Carbon Steel, *Mater. Sci. Eng., A*, 2012, **534**, p 465–475
15. A. Saha, D.K. Mondal, K. Biswas, and J. Maity, Development of High Strength Ductile Hypereutectoid Steel by Cyclic Heat Treatment Process, *Mater. Sci. Eng., A*, 2012, **541**, p 204–215
16. A. Saha, D.K. Mondal, and J. Maity, Effect of Cyclic Heat Treatment on Microstructure and Mechanical Properties of 0.6 wt% Carbon Steel, *Mater. Sci. Eng., A*, 2010, **527**(16–17), p 4001–4007
17. B. Smoljan, An Analysis of Combined Cyclic Heat Treatment Performance, *J. Mater. Process. Technol.*, 2004, **155–156**(1–3), p 1704–1707
18. J.Y. Koo and G. Thomas, Thermal Cycling Treatments and Microstructures for Improved Properties of Fe-0.12% C-0.5% Mn Steels, *Mater. Sci. Eng.*, 1976, **24**(2), p 187–198

19. H.-Y. Li, M.-S. Han, D.-W. Li, J. Li, and D.-C. Xu, Effect of Cyclic Heat Treatment on Microstructure and Mechanical Properties of 50CrV4 Steel, *J. Cent. South Univ.*, 2015, **22**(2), p 409–415
20. Z. Lv, X.-P. Ren, Z.-H. Li, Z.-M. Lu, and M.-M. Gao, Effects of Two Different Cyclic Heat Treatments on Microstructure and Mechanical Properties of Ti-V Microalloyed Steel, *Mater. Res.*, 2015, **18**(2), p 304–312
21. B.R. Kumar, B. Mahato, S. Sharma, and J.K. Sahu, Effect of Cyclic Thermal Process on Ultrafine Grain Formation in AISI, 304L Austenitic Stainless Steel, *Metall. Mater. Trans. A*, 2009, **40A**, p 3226–3234
22. B.R. Kumar and D. Raabe, Tensile Deformation Characteristics of Bulk Ultrafine-Grained Austenitic Stainless Steel Produced by Thermal Cycling, *Scr. Mater.*, 2012, **66**(9), p 634–637
23. S. Tu, X. Ren, B. Nyhus, O.M. Akselsen, J. He, and Z. Zhang, A Special Notched Tensile Specimen to Determine the Flow Stress-Strain Curve of Hardening Materials Without Applying the Bridgman Correction, *Eng. Fract. Mech.*, 2018, **179**, p 225–239
24. S. Kumar, G.P. Chaudhari, S.K. Nath, and B. Basu, Effect of Preheat Temperature on Weldability of Martensitic Stainless Steel, *Mater. Manuf. Process.*, 2012, **27**(12), p 1382–1386
25. Z.L. Zhang, M. Hauge, C. Thaulow, and J. Ødegård, A Notched Cross Weld Tensile Testing Method for Determining True Stress-Strain Curves for Weldments, *Eng. Fract. Mech.*, 2002, **69**(3), p 353–366
26. V. Olden and Z.L. Zhang, *Material Characterisation for Ductile Fracture by Testing of Notched Tensile Specimens, (Cracow), ECF14, 2002*, <https://www.gruppofrattura.it/ocs/index.php/esis/ECF14/scheda/presentations>. Accessed 17 April 2019
27. B. Kishor, G.P. Chaudhari, and S.K. Nath, Slurry Erosion of Thermo-Mechanically Processed 13Cr4Ni Stainless Steel, *Tribol. Int.*, 2016, **93**, p 50–57
28. Y. Wang, M. Chen, F. Zhou, and E. Ma, High Tensile Ductility in a Nanostructured Metal, *Nature*, 2002, **419**, p 912–915
29. F. Ren, F. Chen, and J. Chen, Investigation on Dynamic Recrystallization Behavior of Martensitic Stainless Steel, *Adv. Mater. Sci. Eng.*, 2014, **2014**, p 1–16
30. L.F. Alvarez, C. Garcia, and V. Lopez, Continuous Cooling Transformations in Martensitic Stainless Steels, *ISIJ Int.*, 1994, **34**(6), p 516–521
31. E.I. Galindo-Nava and P.E.J. Rivera-Díaz-Del-Castillo, Understanding the Factors Controlling the Hardness in Martensitic Steels, *Scr. Mater.*, 2016, **110**, p 96–100
32. T. Ohmura, T. Hara, and K. Tsuzaki, Relationship Between Nanohardness and Microstructures in High-Purity Fe-C As-Quenched and Quench-Tempered Martensite, *J. Mater. Res.*, 2003, **18**(6), p 1465–1470
33. A. Akhiate, E. Braud, D. Thibault, and M. Brochu, Carbon Content and Heat Treatment Effects on Microstructures and Mechanical Properties of 13% Cr–4% Ni Martensitic Stainless Steel, *Metall. Mater. Trans. B*, 2014, p 3000–3000
34. H.J. Amarendra, P. Kalhan, G.P. Chaudhari, S.K. Nath, and S. Kumar, Slurry Erosion Response of Heat Treated 13Cr–4Ni Martensitic Stainless Steel, *Mater. Sci. Forum*, 2012, **710**, p 500–505
35. V. Olden, Z.L. Zhang, E. Østby, B. Nyhus, and C. Thaulow, Notch tensile testing of high strength steel weldments, in *2nd International Symposium on High Strength Steel* (Verdal, Norway, 2002), p. 1–8
36. M.A. Maleque, Y.M. Poon, and H.H. Masjuki, The Effect of Intercritical Heat Treatment on the Mechanical Properties of AISI, 3115 Steel, *J. Mater. Process. Technol.*, 2004, **154**, p 482–487
37. L. Morsdorf, O. Jeannin, D. Barbier, M. Mitsuhashi, D. Raabe, and C.C. Tasan, Multiple Mechanisms of Lath Martensite Plasticity, *Acta Mater.*, 2016, **121**, p 202–214
38. S. Zhang, P. Wang, D. Li, and Y. Li, Investigation of the Evolution of Retained Austenite in Fe-13%Cr-4%Ni Martensitic Stainless Steel during Intercritical Tempering, *Mater. Des.*, 2015, **84**, p 385–394
39. M. Moeser, in *Fractography with the SEM (Failure Analysis)*, ed. by J. Bethge and H. Heydnreich (Elsevier Science Ltd, Amsterdam, 1987). <http://www.martin-moeser.de>. Accessed 13 May 2019
40. H. Kitahara, R. Ueji, N. Tsuji, and Y. Minamino, Crystallographic Features of Lath Martensite in Low-Carbon Steel, *Acta Mater.*, 2006, **54**, p 1279–1288
41. S. Morito, H. Yoshida, T. Maki, and X. Huang, Effect of Block Size on the Strength of Lath Martensite in Low Carbon Steels, *Mater. Sci. Eng., A*, 2006, **440**, p 237–240
42. C. Zhang, Q. Wang, J. Ren, R. Li, M. Wang, F. Zhang, and K. Sun, Effect of Martensitic Morphology on Mechanical Properties of an As-Quenched and Tempered 25CrMo48V Steel, *Mater. Sci. Eng., A*, 2012, **534**, p 339–346
43. J.S.J. Hargreaves, Some Considerations Related to the Use of the Scherrer Equation in Powder X-Ray Diffraction as Applied to Heterogeneous Catalysts, *Catal. Struct. React.*, 2016, **2**(1–4), p 33–37
44. G.K. Williamson and R.E. Smallman, III, Dislocation Densities in Some Annealed and Cold-Worked Metals from Measurements on the X-Ray Debye-Scherrer Spectrum, *Philos. Mag.*, 1956, **1**(1), p 34–46
45. G. Krauss, *Steels: Processing, Structure, and Performance*, ASM International, Cleveland, 2005
46. S. Morito, J. Nishikawa, and T. Maki, Dislocation Density Within Lath Martensite in Fe–C and Fe–Ni Alloys, *ISIJ Int.*, 2003, **43**(9), p 1475–1477
47. E.I. Galindo-Nava and P.E.J. Rivera-Díaz-del-Castillo, A Model for the Microstructure Behaviour and Strength Evolution in Lath Martensite, *Acta Mater.*, 2015, **98**, p 81–93
48. H. Nakagawa and T. Miyazaki, Effect of Retained Austenite on the Microstructure and Mechanical Properties of Martensitic Precipitation Hardening Stainless Steel, *J. Mater. Sci.*, 1999, **34**(16), p 3901–3908
49. S. Morito, K. Oh-ishi, K. Hono, and T. Ohba, Carbon Enrichment in Retained Austenite Films in Low Carbon Lath Martensite Steel, *ISIJ Int.*, 2011, **51**(7), p 1200–1202
50. X.D. Wang, N. Zhong, Y.H. Rong, T.Y. Hsu, Z.Y. Xu, and L. Wang, Novel Ultrahigh-Strength Nanolath Martensitic Steel by Quenching–Partitioning–Tempering Process, *J. Mater. Res.*, 2009, **24**(1), p 260–267
51. R. Bhadeshia and H. Honeycombe, *Steels: Microstructure and Properties*, 3rd ed., Butterworth-Heinemann, Oxford, 2006
52. C. Du, J.P.M. Hoefnagels, R. Vaes, and M.G.D. Geers, Block and Sub-block Boundary Strengthening in Lath Martensite, *Scr. Mater.*, 2016, **116**, p 117–121
53. B. Hutchinson and J. Hagstro, Microstructures and Hardness of As-Quenched Martensites (0.1–0.5% C), *Acta Mater.*, 2011, **59**, p 5845–5858
54. Z. Jiang, Z. Guan, and J. Lian, Effects of Microstructural Variables on the Deformation Behaviour of Dual-Phase Steel, *Mater. Sci. Eng., A*, 1995, **190**, p 55–64

**Publisher's Note** Springer Nature remains neutral with regard to jurisdictional claims in published maps and institutional affiliations.